Available online at www.sciencedirect.com
SCIENCE DIRECT®
Acta Materialia 52 (2004) 93–105
Acta MATERIALIA
www.actamat-journals.com

Modeling failure of metallic glasses due to hydrogen embrittlement in the absence of external loads

N. Eliaz [a,*], L. Banks-Sills [b], D. Ashkenazi [a], R. Eliasi [b]

[a] *Biomaterials, Medical Devices & Corrosion Laboratory, Department of Solid Mechanics, Materials and Systems, Tel Aviv University, Ramat Aviv 69978, Israel*

[b] *The Dreszer Fracture Mechanics Laboratory, Department of Solid Mechanics, Materials and Systems, Tel Aviv University, Ramat Aviv 69978, Israel*

Received 22 May 2003; accepted 11 August 2003

Abstract

A model is developed to describe the expansion of high-pressure hydrogen bubbles and propagation of cracks between them in the absence of external loads. The focus is on cracks that form during electrochemical hydrogen charging of amorphous $Fe_{80}B_{11}Si_9$ ribbons. A coupled diffusion/fracture mechanics approach is developed, allowing determination of the time to failure. Finite element analyses are carried out to determine the values of the stress intensity factor for cracks of different lengths, assuming linear elasticity. In addition, the volume of a bubble with edge cracks is related to the internal pressure. The relation between critical pressure and crack length is obtained from an appropriate value of the fracture toughness, K_{Ic}. A criterion is proposed to obtain the pressure and volume as a function of the number of hydrogen moles within the bubble with edge cracks. Finite element analyses are also used to calculate the hydrogen concentration and hydrogen diffusion flux as a function of crack length and time. The time to failure as predicted from this model is of the same order of magnitude as that observed experimentally.

Keywords: Diffusion; Finite element analysis; Fracture; Hydrogen embrittlement; Metallic glasses

1. Introduction

One of the mechanisms that have been proposed to explain the phenomenon of hydrogen embrittlement (HE) in crystalline materials is the high-pressure bubble formation mechanism. According to this model, bubbles filled with molecular hydrogen are formed in various metals having endothermic heats of solution for hydrogen under conditions of high hydrogen fugacity [1]. When the pressure inside the bubble is high enough, the bubble expands. If the level of hydrogen supersaturation is sufficiently high, or if the internal interfaces are weak, microcracks can nucleate and grow even in the absence of an applied stress. The driving force for the propagation of the brittle crack is, thus, the internal pressure in the bubble, or the sum of the external stress and the internal pressure.

Eliaz and Eliezer [2] studied the interaction of hydrogen with amorphous $Fe_{80}B_{11}Si_9$ alloy (numbers in at.%). Scanning electron microscope (SEM) studies revealed microvoids, about 0.4–1.3 μm in diameter, in the cross-section of the uncharged ribbon. These voids were attributed to the processing of the ribbon by rapid solidification. Following electrochemical hydrogen charging in a solution of 0.05 M (0.1 N) H_2SO_4 with 5 g/m^3 $NaAsO_2$ as surface poison and in the absence of any external load, cracks were observed in the ribbons (see Figs. 1(a) and (b)). At high current densities and/or long charging duration, the propagation of interconnecting cracks led to disintegration of the samples in the solution (see Fig. 1(c)). This phenomenon is similar to the general description given by Bockris and Reddy [3]. On the basis of thermal desorption spectroscopy, a value of effective activation energy of hydrogen detrapping was calculated [4] that is similar to the one reported for

* Corresponding author. Tel.: +972-3-640-7384; fax: +972-3-640-7617.
E-mail address: neliaz@eng.tau.ac.il (N. Eliaz).

1359-6454/$30.00 © 2003 Acta Materialia Inc. Published by Elsevier Ltd. All rights reserved.
doi:10.1016/j.actamat.2003.08.029

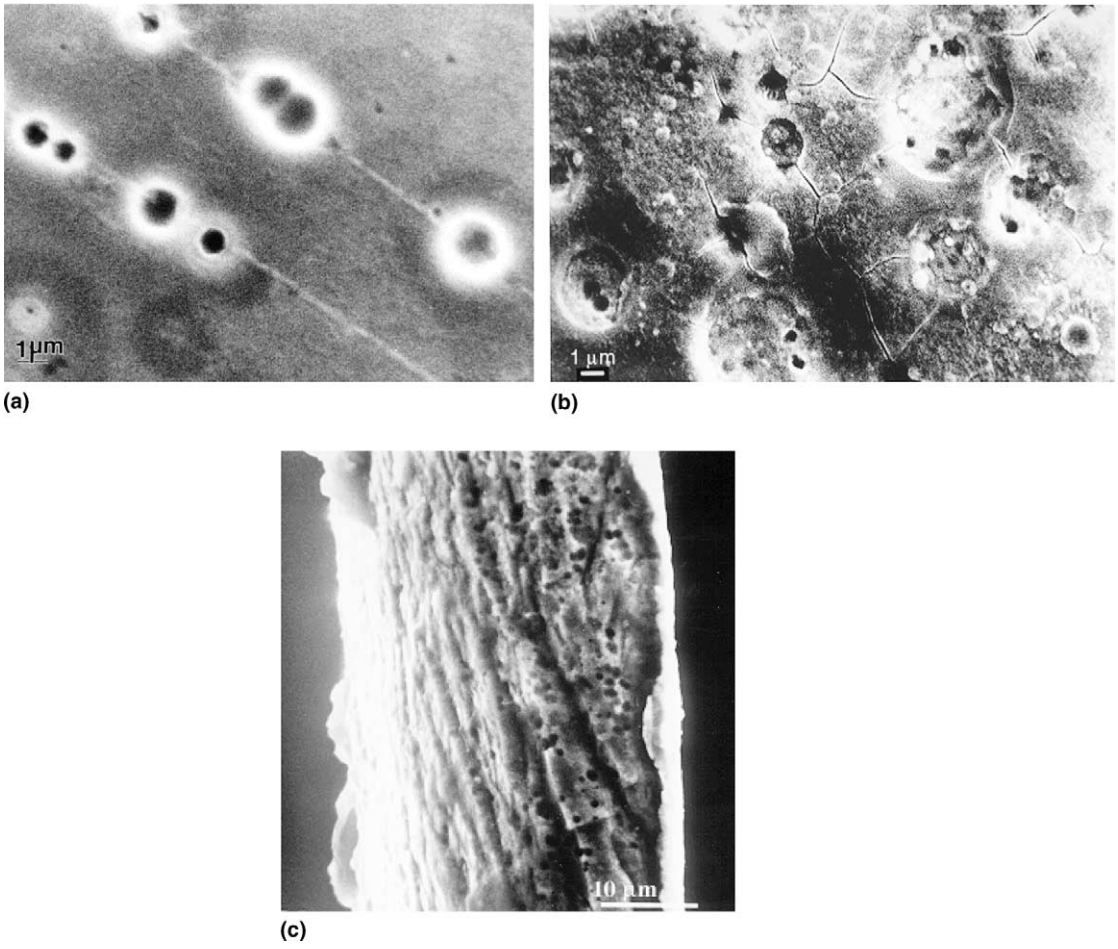

Fig. 1. Scanning electron images demonstrating hydrogen-induced crack propagation in amorphous $Fe_{80}B_{11}Si_9$ [2]: (a) The surface of a ribbon after electrochemical charging at $i_c = 20$ A/m^2 for 30 min. (b) The surface of a ribbon after charging at $i_c = 100$ A/m^2 for 30 min. (c) The fracture surface of a sample shattered during charging at $i_c = 50$ A/m^2.

hydrogen trapping in microvoids in crystalline metals. Laser-induced shock wave measurements also supported the mechanism of high-pressure bubble formation [5].

Finite element analysis has been widely used in many areas of materials science and engineering, mainly because it enables investigation of parameters and boundary conditions which are either difficult or impossible for experimental or analytical study. In addition, it can provide an efficient means for lifetime prediction. Finite element analysis and similar numerical techniques have already been used to model different phenomena related to hydrogen in materials. These phenomena include hydrogen attack in steels [6,7], sulfide stress cracking (SSC) in a steel pipeline [8], hydrogen transport in the neighborhood of a blunting crack tip or a rounded notch under the action of external stresses and related embrittlement phenomena in steels and other materials [9–15], HE resulting from the hydrogen-enhanced localized plasticity mechanism [16], hydrogen transport and elastically accommodated hydride formation near a crack tip [17–19], and slow crack growth in an infinite medium under HE conditions [20].

Unfortunately, the above finite element models are either not applicable or require modification to predict the phenomenon of bubble growth and interconnecting cracks in materials. The two-dimensional model of Schlögl and Van der Giessen [6], for example, does not account for cavity growth and is not successful in predicting the real lifetime of reactors. Krom et al. developed [8] a finite element model for SSC, considering an axisymmetric problem (i.e., a penny-shaped crack). The volume and pressure reached equilibrium through an iteration procedure. The major drawbacks of this model, however, are that it overlooks the mutual effects of existing flaws and incorporates time-consuming iterations.

The objective of this work is to develop a new tool for coupled diffusion/stress analyses aimed at predicting the remnant lifetime of isotropic materials. In this paper, a failure criterion is proposed to determine the time to failure as a result of internal high-pressure bubble formation in metallic glasses. The focus is on cracks that form during electrochemical hydrogen charging of amorphous $Fe_{80}B_{11}Si_9$ ribbons in the absence of external loads. In Section 2, a brief scientific background is

presented, covering the laws of diffusion and hydrogen flux into a bubble. Major parameters required to describe the absorption of hydrogen in a material during electrochemical charging and the non-ideal behavior of hydrogen gas at high pressures are also presented. In Section 3, numerical considerations are described, namely the mesh, geometry and material properties. Several problems with solutions in the literature are solved to demonstrate accuracy of the finite element calculations and examine mesh refinement required for the geometries considered here. In Section 4, stress intensity factors and critical pressure, critical volume and critical number of moles based on a fracture mechanics approach are determined for an isolated bubble as well as a collinear periodic array of bubbles in an infinite strip. In both cases, there are two radial edge cracks emanating from the bubbles. It should be noted that the analyses are two-dimensional and plane strain. The hydrogen concentration profile and flux based on a diffusion approach are employed to calculate the number of gas moles within the bubbles with cracks. These results are coupled with the fracture mechanics analysis to obtain time to failure.

2. Model description

2.1. Hydrogen flux into a bubble

In this investigation, crack propagation between gas bubbles, which form in a metallic glass as a result of an electrochemical process (e.g., cathodic hydrogen charging or electrodeposition) at room temperature is studied. Monoatomic hydrogen is absorbed in the material and diffuses towards microvoids (or microcavities) where it precipitates as molecular hydrogen. This precipitation leads to both pressure buildup within the bubble, so that it expands, and crack growth.

The pressure buildup inside a bubble depends on the flux of hydrogen into it. Under steady-state conditions, the flux vector, $\boldsymbol{J}$, may be described by Fick's first law, namely

$$\boldsymbol{J} = -D\nabla C, \tag{1}$$

where D is the intrinsic (or tracer) diffusion coefficient, C is the concentration of hydrogen, and ∇ is the gradient vector in the direction of mass flow. It should be noted that Eq. (1) does not take into account mass diffusion driven by gradients of stress (or pressure).

The temperature dependence of the diffusion coefficient may be expressed through a simple Arrhenius relation. Under transient conditions, the time-dependent diffusion of hydrogen can be described by Fick's second law, namely

$$\frac{\partial C}{\partial t} = D\nabla^2 C. \tag{2}$$

General solutions of Eq. (2) can be obtained for a variety of initial and boundary conditions provided the diffusion coefficient is constant. For a plane sheet of thickness $2l$ with an initial solute concentration $C_0 = 0$, whose surfaces are maintained at a constant concentration, C_S, the solution of Eq. (2) becomes [21]

$$C = C_S - \frac{4C_S}{\pi}\sum_{n=0}^{\infty}\left[\left(\frac{(-1)^n}{2n+1}\right)\exp\left(\frac{-D(2n+1)^2\pi^2 t}{4l^2}\right)\times\cos\left(\frac{(2n+1)\pi x}{2l}\right)\right]. \tag{3}$$

The solution in Eq. (3) is found by means of a Laplace transform in time. The trigonometric series converges satisfactorily for large values of time.

2.2. Boundary conditions for analysis of hydrogen absorption and diffusion

Fugacity is a measure of deviation from ideal gas behavior and has the same units as pressure. Low-density gases follow the equation-of-state (EOS) for ideal gases $pV = nRT$, where V is the volume, n is the number of gas moles, R is the ideal gas constant (8.3145 J/(mol K)), and T is the absolute temperature. On the other hand, at high pressures gas properties deviate from those of an ideal gas; an EOS for real gases is thus constructed [22,23]. Krom et al. [8] employed a two-term fitting and calculated, using linear regression, a second virial coefficient $B_2 = 5.02 \times 10^{-9}$/Pa at $T = 300$ K. It is claimed that this linear approach is valid at pressures as high as 1 GPa.

The concentration of hydrogen just beneath the outer surface of the ribbon (C_S in Eq. (3)) at a given temperature can be determined if the steady-state permeation flux is measured. This concentration of dissolved (absorbed) hydrogen is proportional to the concentration of adsorbed hydrogen (expressed in terms of surface coverage). However, since such data were not available for the $Fe_{80}B_{11}Si_9$ alloy, a value of $C_S = 1.2 \times 10^5$ mol_H/m^3_{alloy} is used for the numerical analyses.

When the hydrogen pressure inside a bubble reaches a critical value, cracks propagate. The total volume of the bubble and cracks increases, causing the pressure to decrease, with possible crack arrest. The critical number of hydrogen moles necessary for crack propagation may be obtained from the EOS for real gases when the critical pressure in the bubble with cracks and the critical volume are known; that is,

$$\frac{pV}{nRT} = 1 + B_2(T)p. \tag{4}$$

Yet, one has to know under what conditions a crack will first propagate and then arrest, and under what conditions a crack will propagate to failure. To this end, a failure criterion is proposed in this study.

3. Numerical considerations

3.1. Mesh and material properties

In this investigation, two geometries are studied: (a) one bubble with two edge cracks in a rectangular body and (b) a collinear periodic array of bubbles with edge cracks in an infinitely long strip (see Figs. 2(a) and (b), respectively). All bubbles are related to microvoids that were introduced into the material during rapid solidification. The thickness of the strip ($2L_2$ in Figs. 2(a) and (b)) is taken as 25 μm, as measured on the $Fe_{80}B_{11}Si_9$ ribbons that were supplied by AlliedSignal Inc. (Parsippany, NJ) [4,24]. It should be noted that there might be a misunderstanding when defining $2L_2$ as thickness. The ribbon is rotated so that the thickness is in the plane and the width is out of the plane.

A constant initial bubble radius $r_0 = 0.5$ μm is used for all calculations; this radius falls within the size range observed experimentally [2,4]. The surfaces of the bubbles and cracks are subjected to a nominal pressure of $p_0 = 1$ MPa. It should be noted that this pressure, a normalizing factor, is used only in the calculations and is converted to real pressure values (of the order of GPa) in the sequel. The mechanical properties of the amorphous alloy are taken as Young's modulus $E = 110$ GPa [24], Poisson's ratio $v = 0.36$ [25], and fracture toughness $K_{Ic} \sim 10$ MPa$\sqrt{m}$ [26]. The assumptions of linear elasticity and isotropy are both well suited for a metallic glass.

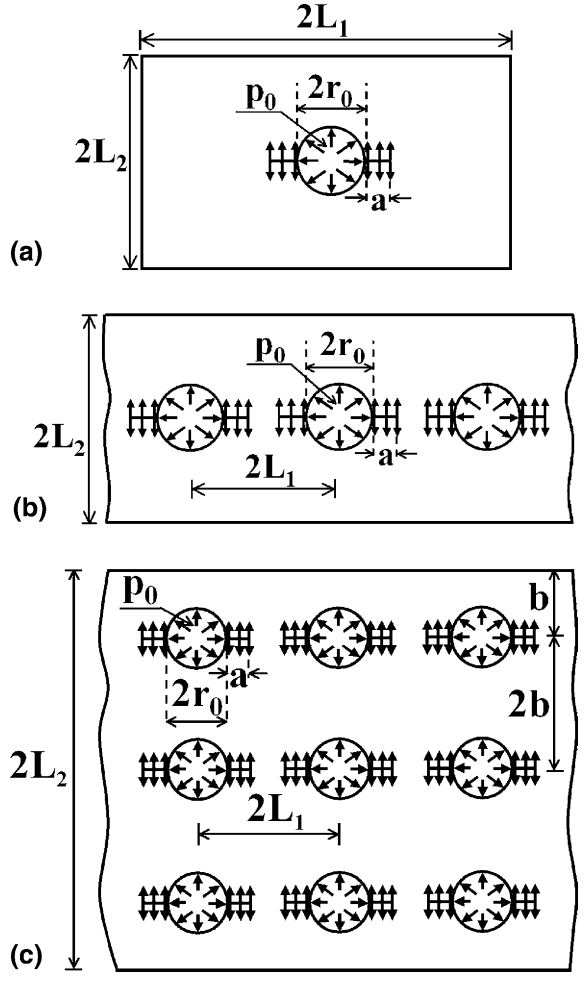

Fig. 2. The three geometries modeled in this study: (a) one bubble with two edge cracks in a rectangular body; (b) a collinear periodic array of bubbles with edge cracks in an infinitely long strip; and (c) three collinear periodic arrays of bubbles with edge cracks in an infinitely long strip.

The geometry is simplified to be of two dimensions so that the bubble is represented as a cylinder. Finite element analyses are carried out under plane strain conditions, using the commercial finite element code ADINA version 7.5.0 [27]. All models are subjected to mode I deformation; so that symmetry conditions allow for modeling one-quarter of the body. The meshes consist of eight-node isoparametric elements. Quarter-point quadrilateral elements are employed at the crack tip to model the stress singularity.

To obtain the stress intensity factors, the conservative J-integral [28] and the virtual crack extension method [27,29] are employed. To avoid confusion, note that this is not the vector $\boldsymbol{J}$ in Eq. (1) which represents the flux. The relation between the mode I dimensional stress intensity factor, K_I, and the J-integral is given by

$$J = \frac{K_I^2}{\bar{E}}, \tag{5}$$

where $\bar{E} = E/(1 - v^2)$ for plane strain conditions. The stress intensity factors are presented in normalized form as

$$\tilde{K}_I = \frac{K_I}{p_0\sqrt{\pi(a + r_0)}}. \tag{6}$$

To further improve the results, overall mesh refinement is pursued. A convergence test shows, in the case of $a/r_0 = 1$ and $L_1/r_0 = 6$ (see Fig. 2(a)), that the values of K_I differ by only 0.1% when using a coarse mesh (1042 elements and 3257 nodes) in comparison to a finer mesh (9666 elements and 29,343 nodes, see Fig. 3). It may be noted that fairly fine meshes are subsequently employed in this study.

3.2. Test problems

In this section, accuracy of the solutions is examined by carrying out several test problems to calculate stress intensity factors and hydrogen concentration. Although for all geometries studied here, in which K_I is calculated, the mechanical properties used are for $Fe_{80}B_{11}Si_9$ (given in the previous subsection), the stress intensity factors do not depend on material properties.

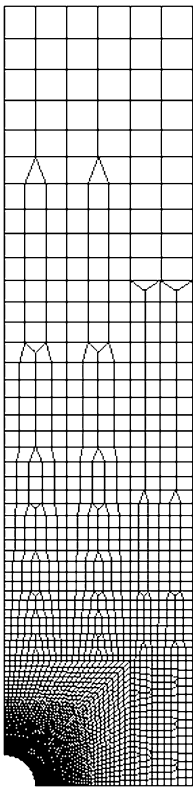

Fig. 3. A typical finite element mesh ($a/r_0 = 0.1$ and $L_1/r_0 = 6$) containing 9666 elements and 29,343 nodal points.

In order to demonstrate accuracy of the finite element model, several comparisons are made to solutions in the literature. Firstly, the case of two radial cracks emanating from a circular hole in an infinite body which is subjected to a far field stress is analyzed. Dimensions as those employed for the bubble with short cracks in the rectangular body in Fig. 2(a) are used here and are sufficient to produce results for an infinite body. The value of K_I obtained from the finite element analysis is only 0.4% higher than the numerical/analytical (mapping) solution of Bowie [30,31].

The second case analyzed consists of two radial cracks at the inner wall of a circular ring loaded with crack face pressure. The ratio of the outer to inner radii is taken to be $r_2/r_1 = 2$, and the normalized crack length $a/r_1 = 0.3$. The value of K_I obtained from the finite element analysis is 0.5% lower than the solution of Andrasic and Parker [32], which was obtained by means of a weight function based on the modified mapping collocation method.

The third test problem consists of a collinear periodic array of cracks along the horizontal axis of an infinite body subjected to a far field tensile stress. This problem is considered to examine mesh refinement required for cracks which approach one another. The thickness (or height) of the repeating cell is taken to be $6L_1$ (see Fig. 2(b)), which is sufficient to produce results for an infinite thickness. For long crack lengths $2a$, the stress intensity factors differ by less than 0.5% as compared to the exact solution [33].

In addition to obtaining stress intensity factors by means of the finite element method, this technique is employed for calculating the hydrogen concentration profile and flux in two cases. Eqs. (1) and (2) together with finite elements are used to calculate the concentration of hydrogen around a bubble and the flux of hydrogen across the bubble surface as a function of crack length and diffusion time. These finite element analyses are carried out using the commercial finite element code ADINA-T version 7.5.0 [27] and a post-processor.

In order to confirm the accuracy of the finite element calculations, two comparisons are made to solutions given in the literature. First, the axisymmetric problem of hydrogen diffusion from the inner wall of a steel pipeline towards an internal penny-shaped crack is analyzed. Material properties and boundary conditions are identical to those employed by Krom et al. [8] in their numerical analysis. Pipeline dimensions are also identical, except one dimension which is not given by Krom et al., while the crack length here is 7.5 mm. The results of these calculations are in good qualitative agreement with those of Krom et al., as long as the assumption of an irreversible hydrogen recombination reaction is made. It may be noted that only qualitative agreement is sought since one of the dimensions is not given by Krom et al. [8]. Next, the problem of non-steady-state diffusion in a plane sheet, whose surfaces are kept at a constant hydrogen concentration, is analyzed for various values of Dt/l^2 where D is the intrinsic diffusion coefficient, t is time and l is the half thickness of the plane sheet. Excellent agreement is found with respect to the analytical results obtained using Eq. (3).

4. Results and discussion

In Section 4.1, a fracture mechanics approach is used to determine stress intensity factors, as well as critical pressure, volume, and number of moles within a bubble with cracks. Two geometries are considered: an isolated bubble within a rectangular body and a collinear periodic array of bubbles. A criterion is proposed to determine conditions for catastrophic failure.

In addition, the diffusion problem is solved numerically. In Section 4.2, the problem is solved by means of the finite element program ADINA-T [27]. The differential diffusion equation in (2) is the same as that for a thermal elastic problem. Analogous variables are identified to carry out the solution of two geometries. The first consists of three parallel collinear periodic arrays of bubbles with cracks within a $Fe_{80}B_{11}Si_9$ ribbon. This problem is employed to demonstrate shielding which

occurs between rows. The second problem is a single collinear periodic array of bubbles with cracks. Here, the diffusion problem is solved, together with the hydrogen flux into the bubbles with cracks. Finally, in Section 4.3, a coupled fracture mechanics/diffusion analysis is carried out. The relation between crack length and time is determined for four bubble spacings and the time to failure for each is obtained.

4.1. Determination of the critical pressure, volume, and number of moles based on a fracture mechanics approach

Meshes with the same order of refinement as those employed in Section 3.2 are used to determine the effective distance between bubble centers below which mutual interaction between the stress fields around the bubbles becomes significant. To this end, the case of a collinear periodic array of uncracked bubbles in an infinitely long strip is analyzed (see Fig. 2(b)), assuming plane strain conditions.

The distances between bubble centers are in the range of 2 μm $\leqslant 2L_1 \leqslant$ 51 μm. The von Mises, or effective, stress given by

$$2\sigma_{\text{eff}}^2 = (\sigma_1 - \sigma_2)^2 + (\sigma_2 - \sigma_3)^2 + (\sigma_3 - \sigma_1)^2, \tag{7}$$

where σ_i, $i = 1, 2, 3$, are the principle stresses, is calculated. It is observed that for distances $L_1 > 5.5$ μm, there is no interaction between the bubbles; that is, σ_{eff}/p_0 at the edge of the bubble nearly does not change at these distances. Recall that the initial bubble radius is $r_0 = 0.5$ μm. Therefore, values of L_1 are chosen to be 1.5, 3, 5.5, and 25.5 μm in this investigation, the latter representing the case of no mutual interaction.

Next, values of the normalized stress intensity factor, $\tilde{K}_{\text{I}}$, are calculated as a function of a/r_0 and L_1/r_0 for the two geometries shown in Figs. 2(a) and (b); recall that Eq. (6) is used to normalize the results. Values are shown in Figs. 4(a) and (b) for the cases of a single bubble with cracks and a collinear periodic array of bubbles with cracks, respectively. As expected, the value of $\tilde{K}_{\text{I}}$ increases with either decreasing L_1/r_0 for a constant crack length, or with increasing crack length for a constant L_1/r_0 ratio. This is expected since as either crack length increases or body dimensions decrease, deviation from the infinite body solution occurs, and in the case of a periodic array of bubbles, mutual interaction between bubbles becomes more significant. In addition, with $L_1/r_0 = 3$, a comparison of stress intensity factors is made in Fig. 5 between the two cases. It may be observed that for small crack lengths, the value of $\tilde{K}_{\text{I}}$ is higher in the case of a periodic array of bubbles with cracks compared to a single bubble with cracks. For

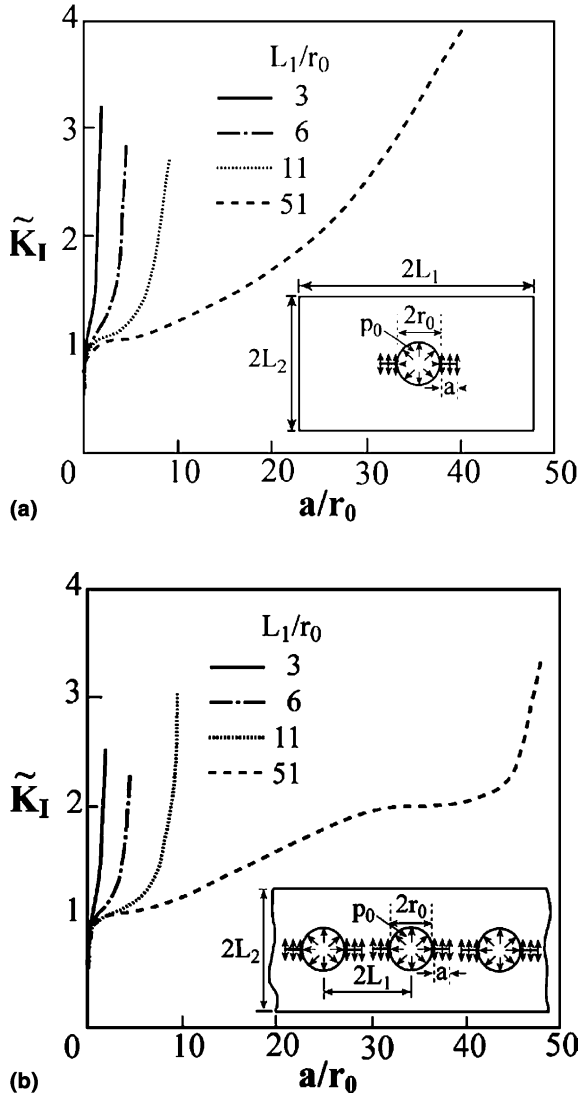

Fig. 4. Dependence of the normalized stress intensity factor on a/r_0 and L_1/r_0 for: (a) one bubble with two edge cracks in a rectangular body and (b) a collinear periodic array of bubbles with edge cracks in an infinitely long strip.

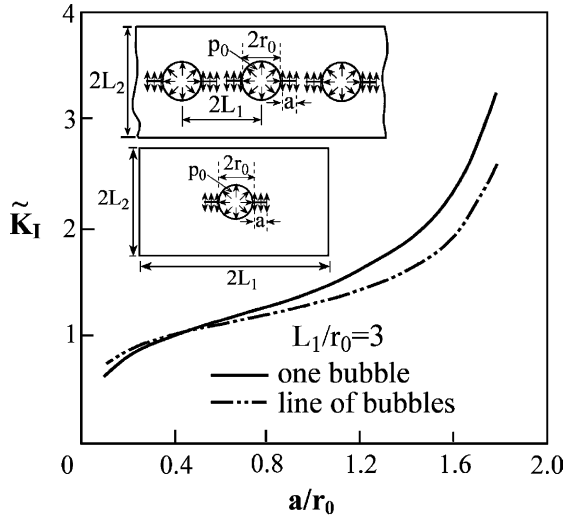

Fig. 5. Comparison of the normalized stress intensity factor for the two geometries shown in Figs. 2(a) and (b) when $L_1/r_0 = 3$.

larger crack lengths (approximately $a/r_0 \geqslant 0.5$ for $L_1/r_0 = 3$), however, this behavior is reversed. The effect of the boundary probably explains the faster increase in $\tilde{K}_I$ in the one-bubble case. Values of $\tilde{K}_I$ are given in Table 1 as a function of normalized crack length, a/r_0, for the case of a periodic array of bubbles with cracks when $L_1/r_0 = 3$.

By equating the calculated values of K_I with the fracture toughness value $K_{Ic} = 10$ MPa$\sqrt{m}$, the critical pressure, p_c, for crack propagation is calculated for each crack length. These values are also presented in Table 1. The dependence of p_c/p_0 on a/r_0 and on the distance between bubble centers is shown in Fig. 6. It is evident that p_c decreases as crack length increases, the decrease being steeper for lower values of L_1/r_0. This dependence may be explained in terms of the dependence of $\tilde{K}_I$ on a and L_1 as shown in Fig. 4(b); higher values of $\tilde{K}_I$ require lower values of pressure for a crack to propagate.

The critical volume, V_c, of a bubble with edge cracks is found from the deformed body for each crack length, at the critical pressure. For a constant value of p_c, higher values of V_c indicate that the ribbon is less susceptible to crack propagation. Normalized values of V_c are presented in Fig. 7 as a function of a/r_0 and L_1/r_0 for the case of a collinear periodic array of bubbles. The critical volume is normalized by the initial volume of the bubble, namely $V_0 = \pi r_0^2 W$. Recall that the bubbles are modeled as cylinders in this two-dimensional analysis; the width $W = 1$ mm is used for the plane strain analysis. From the insert in this figure and for all values of L_1/r_0 it may be observed that V_c initially decreases (at short crack lengths) and then increases. This may at first appear unexpected. But one should note that these results are not calculated as a physically continuous phenomenon. Referring to Table 1, each value of p_c is determined at a specific crack length. Since initially the

Table 1
Relation between crack length, normalized stress intensity factor as well as the critical pressure, volume, and number of hydrogen gas moles for crack propagation

a/r_0	$\tilde{K}_I$	p_c (GPa)	V_c ((μm)^3)	n_c ($\times 10^{-11}$ mol)
0.1	0.701	10.842	1021.0	8.019
0.2	0.867	8.398	979.5	7.654
0.4	1.014	6.644	975.2	7.574
0.6	1.101	5.726	995.3	7.694
0.8	1.179	5.041	1024.0	7.890
1.0	1.268	4.445	1058.0	8.099
1.1	1.322	4.161	1076.0	8.211
1.2	1.386	3.879	1093.0	8.319
1.4	1.559	3.302	1128.0	8.511
1.6	1.855	2.666	1157.0	8.611
1.8	2.544	1.873	1163.0	8.406

The values are obtained from finite element analyses based on a fracture mechanics approach for the case of a collinear periodic array of bubbles with edge cracks in an infinitely long strip. The normalized distance between the centers of two adjacent bubbles is $L_1/r_0 = 3$ (see Fig. 2(b)).

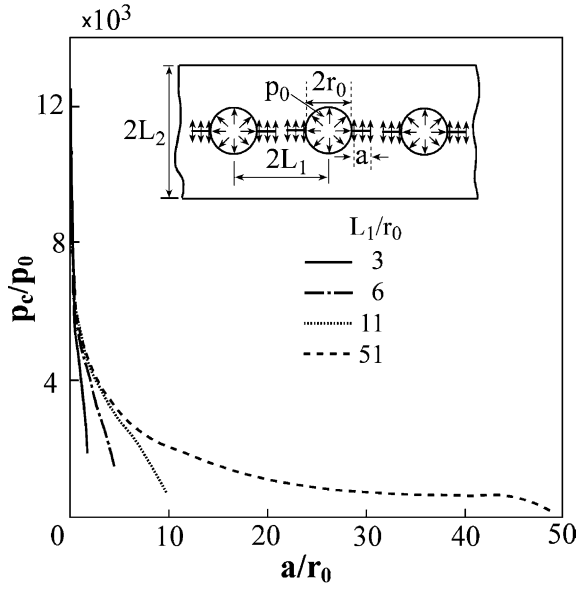

Fig. 6. Dependence of the normalized critical pressure on the crack length to bubble radius ratio and on the distance between bubble centers.

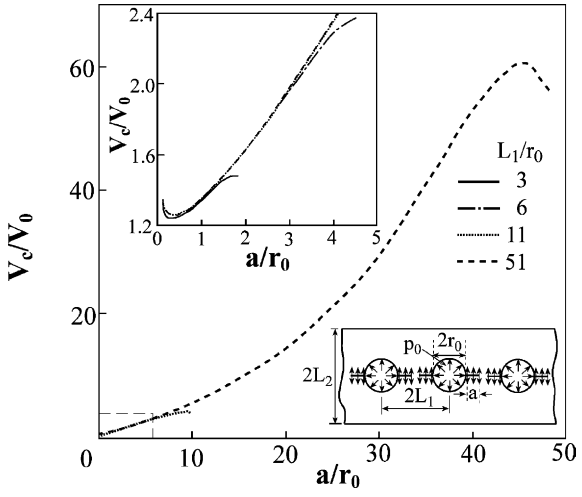

Fig. 7. Values of normalized critical total volume of bubble with edge cracks as a function of a/r_0 and L_1/r_0 for a collinear periodic array of bubbles in an infinitely long strip.

critical pressure decreases significantly, the critical volume, which is obtained from the deformed configuration, also decreases. For $a/r_0 > 0.4$, the decrease in the critical pressure slows and, hence, V_c begins to increase. Interestingly, the minimum in V_c occurs at $a/r_0 \approx 0.4$, close to the location of trend reversal in $\tilde{K}_I$ (see Fig. 5). Moreover, for each value of L_1/r_0 as the crack tips approach one another, either the slope of V_c decreases (for $L_1/r_0 = 3$ and 6) or V_c itself decreases (for $L_1/r_0 = 11$ and 51).

For two extreme bubble spacings ($L_1/r_0 = 3$ and 51), the dependence of the normalized critical volume, V_c/V_0, on the normalized critical pressure, p_c/p_0, is illustrated

in Figs. 8(a) and (b). It should be noted that in Fig. 8(b), the smallest calculated value of p_c/p_0, where V_c/V_0 decreases (according to Fig. 7), has been omitted. The contributions of the bubble volume and the edge crack volume are each presented separately, together with their sum. It is obvious that as p_c increases (i.e., the critical crack length decreases, according to Fig. 6), the critical crack volume decreases. However, the critical total volume depends largely on the critical volume of the bubble itself, as evident from both Figs. 8(a) and (b). At short critical crack lengths (high critical pressures), the critical total volume is essentially equal to the critical bubble volume, while at long crack lengths the relative contribution of crack volume becomes more significant. It may be pointed out that in Fig. 8(a), for example, the bubble volume first decreases as a short crack extends and then remains almost constant for longer crack lengths. This illustrates the observed minimum in Fig. 7.

The relation between p_c/p_0 and V_c/V_0 for different values of L_1/r_0 is presented in Figs. 9(a) and (b) for the one-bubble and line-of-bubbles problems, respectively. These figures clearly demonstrate that for lower values of p_c/p_0 (p_c/p_0 less than about 7200 for the one-bubble case and 9800 for the line-of-bubbles case), at a constant critical pressure, the critical volume increases as L_1 increases. In addition, at a constant critical pressure, the critical volume is greater for a line-of-bubbles as compared to one bubble. As mentioned above, an increased critical volume implies that the specimen will be less susceptible to crack propagation. Thus, shielding occurs for the line-of-bubbles. From Figs. 9(a) and (b) it is also evident that the p_c/V_c behavior nearly does not change when L_1/r_0 is increased from 11 to 51, irrespective of sample geometry. Normalized values of V_c are presented in Table 1 as a function of a/r_0 for a periodic collinear array of bubbles when $L_1/r_0 = 3$.

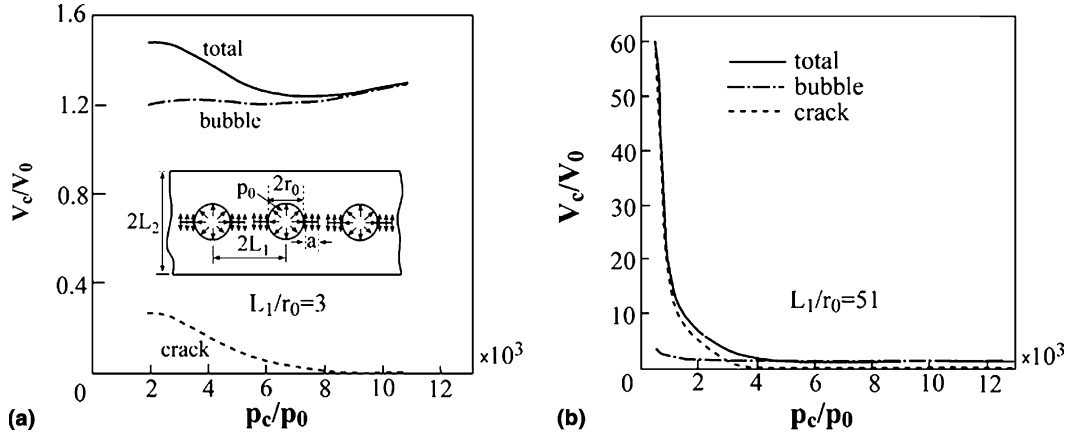

Fig. 8. The p_c dependence of the total critical volume as well as the critical volume of each component of the bubble with edge cracks for: (a) $L_1/r_0 = 3$, and (b) $L_1/r_0 = 51$.

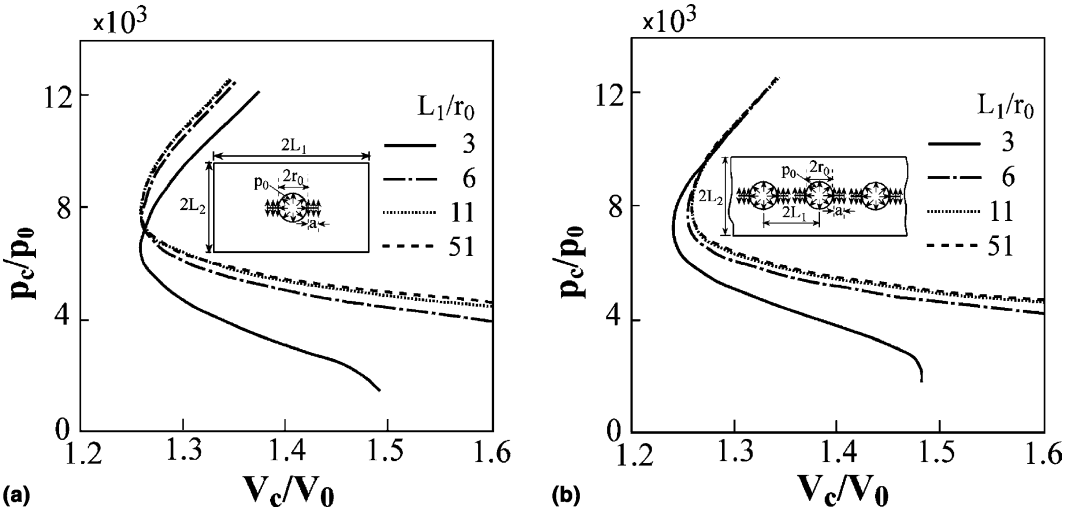

Fig. 9. The relation between the normalized critical pressure and critical volume as a function of L_1/r_0 for: (a) one bubble with two edge cracks in a rectangular body, and (b) a collinear periodic array of bubbles with edge cracks in an infinitely long strip.

The critical number of moles for crack propagation, n_c, may be determined by substituting the values of p_c and V_c into Eq. (4). It may be noted that the calculations are carried out with $T = 300$ K, so that $B_2 = 5.02 \times 10^{-9}$/Pa. The results are plotted in Fig. 10 as a function of a/r_0 and L_1/r_0 for the case of an array of bubbles. The shape of the curves in Fig. 10 is similar to the shape of the normalized volume versus a/r_0 curves (see Fig. 7). A minimum followed by an increase in n_c as a/r_0 increases is observed. In addition, for each value of L_1/r_0 and the highest value of a/r_0 considered, n_c decreases. Values of n_c are presented in Table 1 for $L_1/r_0 = 3$ and the case of a collinear periodic array of bubbles with cracks.

On the basis of Figs. 6–10, it may be concluded that the crack propagation process depends on a variety of parameters, such as the mutual interaction between bubbles, the geometry and dimensions of the specimen, the length of the crack relative to the bubble size, and the number of hydrogen moles within the bubbles and cracks.

A failure criterion is proposed in the framework of this investigation to predict crack propagation and possible arrest. As an example, consider a collinear periodic array of bubbles with $L_1/r_0 = 3$; there is interaction between the bubbles. It is initially assumed that only small cracks with $a/r_0 = 0.1$ are present. As the hydrogen flows into the bubbles with cracks, the pressure and volume increase until a critical pressure is reached and the cracks begin to propagate. The critical pressure is obtained from fracture mechanics theory by comparing K_I to K_{Ic}. At this pressure, the critical volume is obtained from a finite element analysis in which the deformation of the bubble with cracks is determined. For this critical pressure and volume, the critical number of hydrogen moles $n_c = 8.02 \times 10^{-11}$ mol is obtained from the EOS given in Eq. (4); the exact numbers are presented in Table 1.

As the cracks propagate, which is assumed to be a quasi-static phenomenon, the number of moles for continued propagation is lower than n_c (see Table 1); thus, the cracks grow until $a/r_0 = 1.0$. Assuming that the number of moles has not increased, the cracks then arrest. Fig. 11 may be examined to determine continued crack growth. Finite element analyses are carried out with $a/r_0 = 1.0$ to determine a relation between the pressure within the bubble and cracks and their volume. Note that only one finite element analysis is necessary since the relation between pressure and displacement is linear. This curve is plotted in Fig. 11 as the 'deformation relation'; it is slightly nonlinear (volume is a nonlinear function of pressure). The other curve is obtained from the EOS given in Eq. (4) with $n = 8.02 \times 10^{-11}$ mol, the value that is calculated for the smallest initial crack length of $a/r_0 = 0.1$, and labeled 'gas equation' in Fig. 11. The intersection point of both curves is defined as p_s ($p_s/p_0 = 4.310$). For this particular geometry, the normalized critical pressure may be found as $p_c/p_0 = 4.445$ (see Table 1, $a/r_0 = 1.0$) as shown in Fig. 11. Here $p_s < p_c$ so that the cracks will not propagate. As the number of moles increases, the pressure and volume

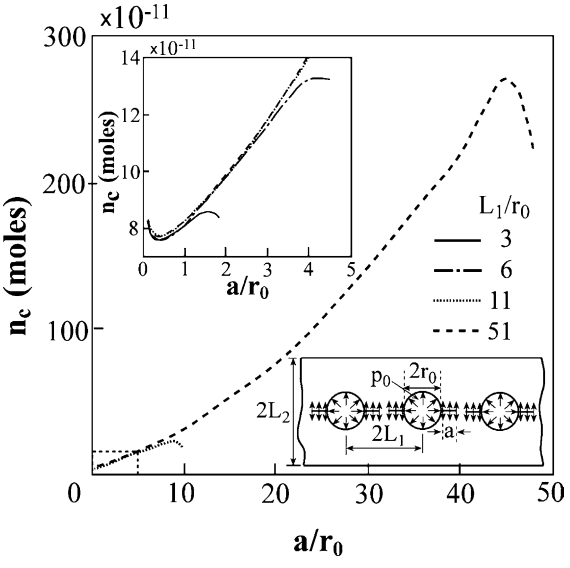

Fig. 10. The critical number of moles for crack propagation, obtained on the basis of a fracture mechanics approach, as a function of a/r_0 and L_1/r_0 for a collinear periodic array of bubbles.

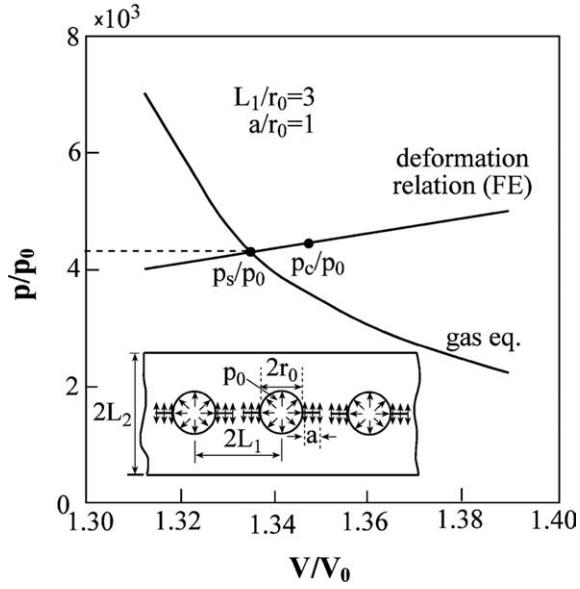

Fig. 11. A schematic presentation of a failure criterion, which is based upon the change in pressure as a function of the total volume of a bubble with two edge cracks within a collinear periodic array of bubbles with cracks. The elastic solution obtained from finite element analysis is plotted together with the EOS for a real gas (Eq. (4)). In this graph, $p_s/p_0 = 4.310$, $p_c/p_0 = 4.445$, and $n = 8.02 \times 10^{-11}$ mol. Since $p_s < p_c$, the crack will arrest until the number of hydrogen moles inside the bubble with cracks reaches the critical value.

increase along the 'deformation relation'. The curve labeled 'gas equation' moves up and to the right, so that the intersection point increases, until p_c is reached and the crack propagates. As the crack grows, the pressure decreases and may fall below p_c; so that the crack arrests. Hydrogen continues to diffuse into the bubble with cracks until a critical value of moles is reached. This process repeats itself until the glassy ribbon fails.

4.2. Determination of the hydrogen concentration profile, hydrogen flux, and number of gas moles in a bubble based on a diffusion approach

Initially, the problem of three collinear periodic arrays of bubbles with cracks is considered (as illustrated in Fig. 2(c)). To this end, the differential equation for diffusion, Eq. (2), is solved incrementally by means of the finite element method (ADINA-T [27]). The dimensions of the body are $L_1/r_0 = 11$, $L_2/r_0 = 25$, $a/r_0 = 2$ and the vertical distance between bubble centers $b/r_0 = 8.33$. The mesh of one-quarter of a unit cell consists of 11,060 elements and 33,713 nodes (see Fig. 12(a)). The boundary condition on the outer surface of the ribbon is given by $C_S = 1.2 \times 10^5$ mol_H/m^3_{alloy}. A diffusion coefficient $D = 1.22 \times 10^{-14}$ m^2/s is taken as typical for amorphous Fe–Si–B alloys at 300 K [4]. The assumption of an irreversible hydrogen recombination reaction is made. The normal derivative of the concentration is zero along the connecting boundaries of the unit cell, namely AB, CD, EF, FG. The resulting concentration profile is shown in Fig. 12(b). From this figure it is evident that the first line of bubbles with edge cracks, which is closest to the outer surface of the specimen, acts as an unsaturable trap and attracts much hydrogen from the surrounding material. Consequently, hydrogen concentration around the second (inner) line of bubbles is too low to allow simultaneous crack propagation. A similar "shielding effect" was observed by Krom et al. [8] for hydrogen distribution through the wall of a steel pipe. Thus, in order for a network of interconnecting cracks to propagate through the thickness of the amorphous ribbon, it is required that microvoids be distributed in an asymmetric manner and/or new unshielded paths for diffusion of hydrogen from the outer surface should form during the process.

Next, a single collinear array of bubbles in Fig. 2(b) is considered. Here, in addition to solving the diffusion equation, other parameters are obtained. A finite element model is created of one-quarter of a unit cell for the geometry in Fig. 2(b). The same boundary conditions as described in the previous problem are employed. The time increment is taken as 2 s. It should be noted that this time step is found to be satisfactory for convergence. For example, for a total time of 600 s, the number of moles within the cracked bubbles calculated using a time increment of 2 s is only 1.3% higher than the number of moles calculated using a time increment of 0.5 s. The hydrogen concentration, C, at the edge of the bubble with cracks is found and employed in Eq. (1) to obtain the flux of hydrogen, $\boldsymbol{J}$, across the bubble and

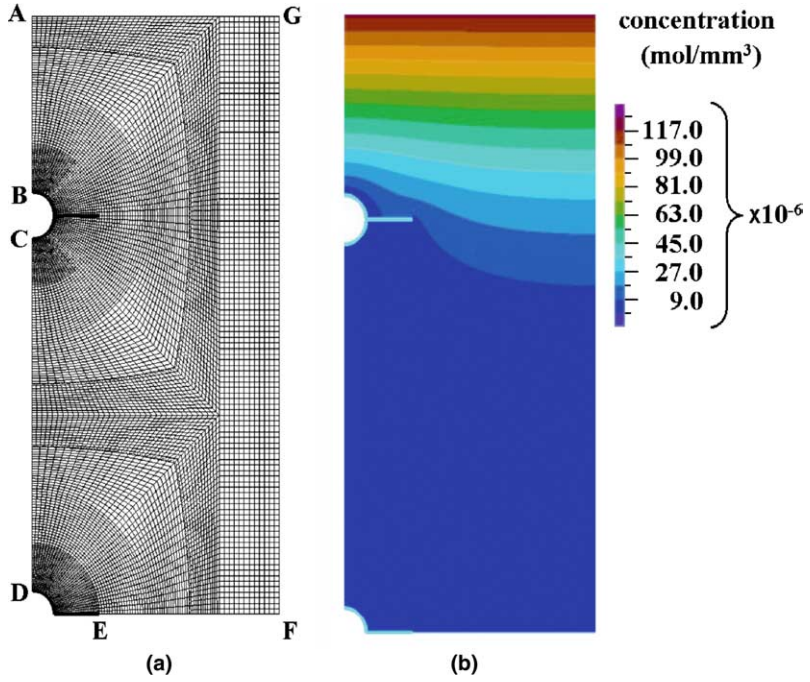

Fig. 12. (a) Mesh of one-quarter of a unit cell for the geometry shown in Fig. 2(c) consisting of 11,060 elements and 33,713 nodes ($L_1/r_0 = 11$, $L_2/r_0 = 25$, $a/r_0 = 2$, and $b/r_0 = 8.33$). (b) The resulting hydrogen concentration profile, demonstrating a "shielding effect" caused by the collinear periodic array of bubbles with edge cracks, which is closest to the outer surface of the specimen.

crack surfaces. The number of hydrogen gas moles, n, inside the bubble with cracks is determined as the product of diffusion flux, surface area of bubble with cracks, and time increment. This procedure is repeated for increasing time.

After a diffusion time of 1400 s, the number of hydrogen gas moles inside a bubble with cracks is obtained as a function of the non-dimensional crack length and the distance between centers of adjacent bubbles; it is presented in Fig. 13. For a given bubble spacing L_1/r_0 the number of gas moles is found to increase monotonically with crack length. This is expected for the irreversible reaction of gas precipitation in a growing crack (i.e., growing volume). In addition, as the distance between bubbles decreases, the number of moles decreases too. This may be explained in terms of the need to fill simultaneously several traps with mutual interactions.

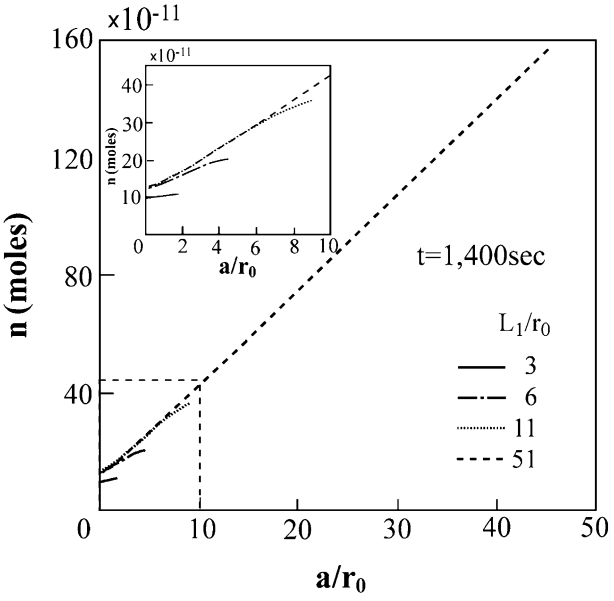

Fig. 13. The number of hydrogen gas moles inside a bubble with cracks after a diffusion time of 1400 s as a function of the non-dimensional crack length and the distance between adjacent bubble centers.

The dependence of the number of hydrogen gas moles inside a bubble on the diffusion time and crack length is shown in Figs. 14(a) and (b) for $L_1/r_0 = 3$ and $L_1/r_0 = 51$, respectively. As crack length and volume increase, the number of hydrogen gas moles increases, as expected. Moreover, it is evident that for the same crack length, the number of hydrogen gas moles inside a bubble with cracks increases with the distance between bubbles. Note the differing scales in the two plots. The dependence of the number of moles on crack length after various diffusion times is presented in Table 2 for a collinear periodic array of bubbles with cracks and $L_1/r_0 = 3$.

4.3. Coupled fracture mechanics/diffusion analysis

By coupling the fracture mechanics and diffusion analyses, one may calculate the time necessary to attain the critical number of hydrogen gas moles inside a bubble with cracks, which will lead to crack propagation. Thus, the time to failure can be predicted. The dependence of crack length on diffusion time is illustrated in Fig. 15 for a collinear periodic array of bubbles with cracks for various values of L_1/r_0. It may be observed that an incubation period exists before the crack is filled with sufficient hydrogen gas to allow for propagation. Subsequently, except for $L_1/r_0 = 3$, in which a constant slope may be observed, the crack propagation rate cannot be claimed to be constant as determined by Krom et al. [8].

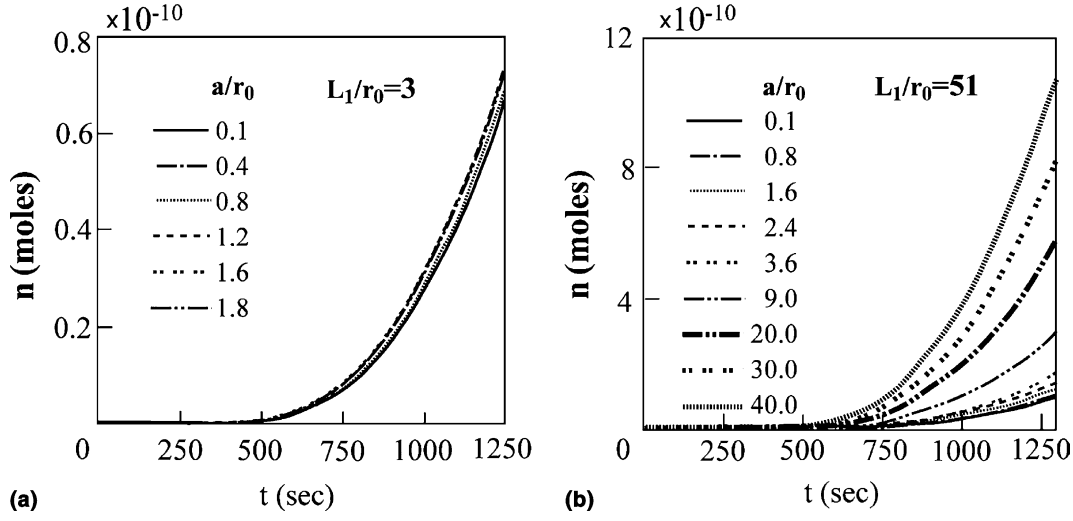

Fig. 14. The dependence of the number of hydrogen gas moles inside a cracked bubble on the diffusion time and crack length for: (a) $L_1/r_0 = 3$ and (b) $L_1/r_0 = 51$. Results are for a collinear periodic array of cracked bubbles in Fig. 2(b).

Table 2
The number of hydrogen gas moles inside a bubble with cracks as a function of crack length and diffusion time

a/r_0	t (s)				
	400	800	1200	1300	1400
0.1	8.193×10^{-14}	9.161×10^{-12}	5.639×10^{-11}	7.612×10^{-11}	9.905×10^{-11}
0.2	8.239×10^{-14}	9.189×10^{-12}	5.648×10^{-11}	7.623×10^{-11}	9.917×10^{-11}
0.4	8.423×10^{-14}	9.323×10^{-12}	5.705×10^{-11}	7.694×10^{-11}	1.000×10^{-10}
0.6	8.665×10^{-14}	9.498×10^{-12}	5.780×10^{-11}	7.787×10^{-11}	1.012×10^{-10}
0.8	8.933×10^{-14}	9.686×10^{-12}	5.858×10^{-11}	7.886×10^{-11}	1.023×10^{-10}
1.0	9.227×10^{-14}	9.896×10^{-12}	5.951×10^{-11}	8.002×10^{-11}	1.038×10^{-10}
1.1	9.377×10^{-14}	1.000×10^{-11}	6.000×10^{-11}	8.065×10^{-11}	1.045×10^{-10}
1.2	9.670×10^{-14}	1.026×10^{-11}	6.140×10^{-11}	8.249×10^{-11}	1.069×10^{-10}
1.4	9.830×10^{-14}	1.034×10^{-11}	6.164×10^{-11}	8.276×10^{-11}	1.072×10^{-10}
1.6	9.990×10^{-14}	1.042×10^{-11}	6.188×10^{-11}	8.303×10^{-11}	1.075×10^{-10}
1.8	1.016×10^{-13}	1.055×10^{-11}	6.251×10^{-11}	8.386×10^{-11}	1.085×10^{-10}

The values are obtained from a diffusion analysis, by means of the finite element method, for a collinear periodic array of bubbles with edge cracks in an infinitely long strip, where the normalized distance between the centers of two adjacent bubbles is $L_1/r_0 = 3$ (see Fig. 2(b)).

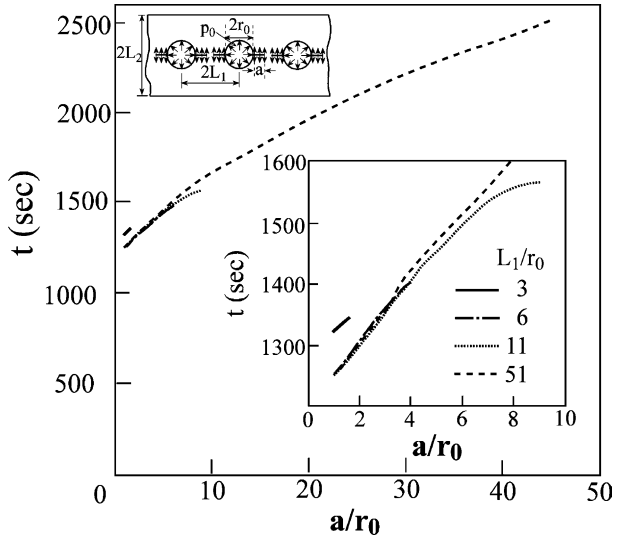

Fig. 15. The dependence of diffusion time on crack length for the case of a collinear periodic array of bubbles with cracks and various values of L_1/r_0.

An example of the procedure employed for determining the time to failure is presented for $L_1/r_0 = 3$. Reference is made to Table 1, with the initial crack length $a/r_0 = 0.1$. The time is calculated to reach $n_c = 8.019 \times 10^{-11}$ mol. Recall that the finite element program ADINA-T [27] is employed with time steps of $\Delta t = 2$ s. In Table 2, some values are given relating the time it takes for a certain number of moles to fill the bubbles and cracks. For $a/r_0 = 0.1$, the value of n_c (from Table 1) is found between $t = 1300$ and 1400 s. More detailed tables are employed in the calculation. In the region of n_c, a parabola is fitted between 12 points of 2 s intervals by least squares to give a good approximation of the time. For $a/r_0 = 0.1$, the time is found as $t = 1,318.8$ s. Referring to Table 1, since the critical numbers of moles for crack lengths $0.1 < a/r_0 < 1.0$ are less than that for $a/r_0 = 0.1$, the crack propagates until $a/r_0 = 1.0$ is reached. The critical number of moles for crack growth at this length is $n_c = 8.099 \times 10^{-11}$ mol. Hence, time elapses until sufficient hydrogen diffuses into the bubbles and cracks for the cracks to propagate again. For each crack length, a separate least-squares fit of 12–15 points to a parabola around the new number of moles required for propagation allows for calculation of the related time increment. For example, with $a/r_0 = 1.0$, $\Delta t = 3.6$ s. Continuing in this way, the time to failure is obtained as $t_f = 1345$ s. In a similar manner, the time to failure is obtained for other bubble spacings. For $L_1/r_0 = 6$, the time to failure is 1402 s; for $L_1/r_0 = 11$, $t_f = 1569$ s; for $L_1/r_0 = 51$, $t_f = 2507$ s. For all bubble spacings, failure time is easily attained since the critical number of moles decreases as crack tips approach. This may be observed in Table 1 for $L_1/r_0 = 3$ with $a/r_0 = 1.6$ and 1.8.

For comparison, Eliaz and Eliezer [2,4] electrochemically charged $Fe_{80}B_{11}Si_9$ ribbons. Interconnecting cracks on the surface of the ribbons were detected after 1800 s of charging at $i_c = 20$ A/m^2 (Fig. 1(a)). Thus, the new coupled diffusion/stress finite element model that is developed herein provides a reasonable fit with this experimental data.

4.4. Discussion

There are various modifications that may be made to further improve the present model. Firstly, additional arrangements of microvoids (e.g., doubly periodic and zig-zag periodic arrays of voids with cracks) should be studied. Secondly, additional microvoid sizes (mainly, using a normal distribution of void diameters) should be investigated to better simulate the experimental microscopic observations. Thirdly, one may take into account equilibrium between diffusion and trapping of hydrogen, hydrogen diffusivity which is concentration and pressure dependent, and hydrogen effects on the local values of

the elastic constants as well as on stress relaxation. In addition, a three-dimensional model may be developed. Finally, electrochemical permeation experiments should be carried out to define more accurately the boundary condition of C_S.

The model presented here may be extended to other failure mechanisms as well. For example, a similar approach may be utilized to predict the synergistic effects of helium and hydrogen in isotropic and anisotropic crystalline metals. In order to model these effects properly, one has to take into account not only diffusion and trapping phenomena, but also the mutual effects of helium bubbles, or the effect of the stress fields around helium bubbles on the diffusion and degradation processes. Such a model may be useful in the selection process of materials for the first wall of thermonuclear fusion reactors.

5. Conclusions

In this study, a coupled fracture mechanics/diffusion approach was developed to model the failure of metallic glasses resulting from hydrogen embrittlement in the absence of external loads. It was employed to predict the time to failure of amorphous $Fe_{80}B_{11}Si_9$ ribbons in which high-pressure bubble formation and interconnecting crack propagation occur during electrochemical hydrogen charging. The following conclusions may be drawn:

1. The crack propagation process depends on a variety of parameters, such as the mutual interaction between bubbles, the geometry and dimensions of the specimen, and the length of the crack relative to the bubble size.
2. The intersection point between the p–V curves for the fracture mechanics-based elastic solution and for the EOS of real hydrogen gas may be used, in conjunction with the value of the critical pressure, as a failure criterion.
3. Crack propagation is characterized by the existence of an incubation period in which the hydrogen first fills the bubbles and cracks until a critical pressure is attained. Subsequently, the rate of crack propagation to failure is not constant except when $L_1/r_0 = 3$.
4. In the absence of mutual interaction between stress fields around adjacent bubbles, gas accumulation in bubbles is faster.
5. Based on comparisons to a variety of analytical and numerical solutions for different problems, the accuracy of the new model is high.
6. The time to failure, as predicted by this model, is similar to that observed experimentally.
7. The model presented herein can be extended to other failure mechanisms and may be useful in the process of materials selection.

References

[1] Tetelman S, Robertson WD. Trans AIME 1962;224:775.
[2] Eliaz N, Eliezer D. Metall Mater Trans A 2000;31A:2517.
[3] Bockris JO'M, Reddy AKN. In: Modern electrochemistry, vol. 2. New York, NY: Plenum Press; 1970. p. 1328.
[4] Eliaz N. Hydrogen interaction with amorphous and quasicrystalline alloys. Ph.D. Thesis, Ben-Gurion University, Israel, June 1999.
[5] Eliaz N, Moshe E, Eliezer S, Eliezer D. Metall Mater Trans A 2000;31A:1085.
[6] Schlögl SM, Van der Giessen E. Scripta Mater 2002;46:431.
[7] Schlögl SM, Svoboda J, Van der Giessen E. Acta Mater 2001; 49:2227.
[8] Krom AHM, Bakker A, Koers RWJ. Int J Pres Ves Piping 1997;72:139.
[9] Taha A, Sofronis P. Eng Fract Mech 2001;68:803.
[10] Lufrano J, Sofronis P. Acta Mater 1998;46(5):1519.
[11] Sofronis P, Lufrano J. Mater Sci Engrg A 1999;A260:41.
[12] Lufrano J, Sofronis P, Symons D. Eng Fract Mech 1998;59(6):827.
[13] Lufrano JM, Sofronis P. TAM Report No. 771, University of Illinois at Urbana-Champaign, October 1994.
[14] Sofronis P, McMeeking RM. J Mech Phys Solids 1989;37(3):317.
[15] Toshimitsu Yokobori A, Nemoto T, Satoh K, Yamada T. Eng Fract Mech 1996;55(1):47.
[16] Sofronis P, Robertson I.M. TAM Report No. 972, University of Illinois at Urbana-Champaign, June 2001.
[17] Lufrano J, Sofronis P, Birnbaum HK. J Mech Phys Solids 1998;46(9):1497.
[18] Lufrano J, Sofronis P, Birnbaum HK. J Mech Phys Solids 1996;44(2):179.
[19] Varias AG, Massih AR. J Nucl Mater 2000;279:273.
[20] Goldstein RV, Balueva AV. Fatigue Fract Eng Mater Struct 1997;20(9):1269.
[21] Crank J. The mathematics of diffusion. 2nd ed. Oxford, UK: Clarendon; 1975. p. 44.
[22] Dymond JH, Smith EB. The virial coefficients of pure gases and mixtures: a critical compilation. Oxford: Clarendon Press; 1980. p. 199.
[23] Atkins P, de Paula J. Atkins' physical chemistry. 7th ed. Oxford, UK: Oxford University Press; 2002. p. 127.
[24] AlliedSignal Inc., Metglas 2605SA1. Technical Bulletin, Parsippany, NJ, 1995.
[25] Chen HS. J Appl Phys 1978;49(1):462.
[26] Lin J-J, Perng T-P. Mater Sci Lett 1991;10:1443.
[27] Bathe KJ. ADINA (version 7.5.0) – automatic dynamic incremental nonlinear analysis: theory and modeling guide. Watertown, MA: ADINA Engineering; 2001.
[28] Rice JR. J Appl Mech 1968;35:379.
[29] Parks DM. Int J Fract 1974;10:487.
[30] Bowie OL. J Math 1956;XXXV(1):60.
[31] Murakami Y, editor. Stress intensity factors handbook, vol. 1. Oxford: Pergamon Press; 1987. p. 239.
[32] Andrasic CP, Parker AP. Eng Fract Mech 1984;19(1):187.
[33] Irwin GR. In: Flugge S, editor. Encyclopedia of physics. sixth ed. Berlin: Springer-Verlag; 1958. p. 565.